*Nano Research* 2015, 8(4): 1339–1347
DOI 10.1007/s12274-014-0625-6
**Research Article**

ISSN 1998-0124
CN 11-5974/O4

# Improving the electrochemical performance of $Fe_3O_4$ nanoparticles via a double protection strategy through carbon nanotube decoration and graphene networks

Shuliang Yang, Changyan Cao (✉), Gen Li, Yongbin Sun, Peipei Huang, Fangfang Wei, and Weiguo Song (✉)

*Beijing National Laboratory for Molecular Sciences, Laboratory of Molecular Nanostructures and Nanotechnology, Institute of Chemistry, Chinese Academy of Sciences, Beijing 100190, China*

**Received:** 10 August 2014
**Revised:** 8 October 2014
**Accepted:** 28 October 2014

## KEYWORDS

$Fe_3O_4$,
carbon nanotube,
graphene,
lithium ion batteries,
anode materials

## ABSTRACT

Iron oxide is a promising anode material for lithium ion batteries, but it usually exhibits poor electrochemical property because of its poor conductivity and large volume variation during the lithium uptake and release processes. In this work, a double protection strategy for improving electrochemical performance of $Fe_3O_4$ nanoparticles through the use of decoration with multi-walled carbon nanotubes and reduced graphene oxides networks has been developed. The resulting MWCNTs–$Fe_3O_4$–rGO nanocomposites exhibited excellent cycling performance and rate capability in comparison with MWCNTs–$Fe_3O_4$, MWCNTs–$Fe_3O_4$ physically mixed with rGO, and $Fe_3O_4$–rGO. A reversible capacity of ~680 mA·h·g$^{-1}$ can be maintained after 100 cycles under a current density of 200 mA·g$^{-1}$.

## 1 Introduction

Due to the growing demand for high energy and power density of Li-ion batteries (LIB), transition metal oxides have gained continuing research interest for their higher specific capacity comparing to graphitic anodes with theoretical capacity of 372 mA·h·g$^{-1}$ [1–5]. Among them, $Fe_3O_4$ is considered as a more promising anode material candidate than other oxides because of its high theoretical capacity of 922 mA·h·g$^{-1}$, low cost, being environmentally benign, and its high natural abundance [6, 7]. However, $Fe_3O_4$-based anode materials often suffer from poor cycling performance and low rate capability due to large specific volume changes upon cycling and the intrinsic kinetic limitations of $Fe_3O_4$. To address these issues, various strategies have been developed to improve the structural integrity and electrical conductivity of $Fe_3O_4$-based materials. These methods can be divided into two main categories: One is to synthesis of $Fe_3O_4$ nanostructures with optimized particle size or morphology [6, 8, 9]; the other one is to combine $Fe_3O_4$ with conductive

---

Address correspondence to Changyan Cao, cycao@iccas.ac.cn; Weiguo Song, wsong@iccas.ac.cn

substrates (such as graphene [10–20] or carbon shells [21–24]) to fabricate $Fe_3O_4$/carbon composites. Here, we have combined these two approaches and produced a MWCNTs–$Fe_3O_4$–rGO nanocomposite material with excellent electrochemical properties.

As the impressive representatives of carbon nanomaterials, carbon nanotubes (CNTs) [25–27] and graphene [28–32] have been widely used in the field of energy storage due to their high electrical conductivity, large surface area, and chemical stability. In previous reports, $Fe_3O_4$ nanoparticles were directly decorated on graphene to use as Li-ion anodes. However, the loaded $Fe_3O_4$ nanoparticles will detach from the graphene easily if there is no protection layer, which will further cause the decay of capacity during the cycle process [19, 20]. Although much progress has been obtained for $Fe_3O_4$–graphene composites, the use of CNTs-based $Fe_3O_4$ for Li-ion batteries has rarely been reported [33, 34]. A possible reason may be the chemically inert feature of CNTs, making it difficult to uniformly disperse $Fe_3O_4$ directly. High temperature treatment with concentrated acid or doping with heteroatoms has usually been adopted to functionalize the surface first [35–37]. However, these methods generate waste acid and are also time-consuming. Moreover, the resulting introduction of defects and functional groups destroys the conjugated structure system of CNTs, which further affects the electronic conductivity of CNTs. Therefore, developing a facile method to synthesize CNTs–$Fe_3O_4$ without any pretreatment of the CNTs is desirable. Moreover, wrapping CNTs–$Fe_3O_4$ with graphene to form mixed conducting 3D networks may further enhance the electrochemical properties of the $Fe_3O_4$ nanoparticles.

Based on these ideas, we have developed a double protection strategy for improving both the cyclability and rate capability of $Fe_3O_4$ nanoparticles through the use of decoration with multi-walled carbon nanotubes (MWCNTs) and the formation of reduced graphene oxides (rGO) networks. $Fe_3O_4$ nanoparticles with diameter of ca. 7 nm are first decorated directly onto the surface of MWCNTs without any pretreatment, forming conductive wires. Elastic rGO networks are then introduced to wrap the MWCNTs–$Fe_3O_4$ to form MWCNTs–$Fe_3O_4$–rGO nanocomposites, which not only provide a highly conductive network for electron transfer during the lithiation and delithiation processes, but also serve as a buffer to alleviate the aggregation and volume changes of $Fe_3O_4$ nanoparticles. When used as an anode material for Li-ion batteries, MWCNTs–$Fe_3O_4$–rGO nanocomposites exhibit much-improved electrochemical performance in comparison with MWCNTs–$Fe_3O_4$ and MWCNTs–$Fe_3O_4$ physically mixed with rGO.

## 2 Experimental

### 2.1 Sample preparation

#### 2.1.1 *Synthesis of MWCNTs–$Fe_3O_4$ (F-1)*

In a typical procedure, 700 mg of Fe(acac)$_3$ and 80 mg MWCNTs were added to a 100 mL flask containing 48 mL of triethylene glycol (TREG). After ultrasonication for 10 min, the resulting solution was rapidly heated to 190 °C under argon protection, maintained there for 30 min, and then heated rapidly to 278 °C, and held there for an additional 30 min. After cooling to room temperature, the obtained mixture was centrifuged and washed five times with ethyl acetate and dried in vacuum at room temperature for 6 h.

#### 2.1.2 *Synthesis of MWCNTs–$Fe_3O_4$–rGO (F-2)*

Firstly, graphene oxide (GO) solution was prepared through mixing 5 mL of 5 mg/mL GO with 10 mL of ethylene glycol. The obtained MWCNTs–$Fe_3O_4$ was stirred directly with the above-mentioned GO solution for 1.0 h. Then, the mixture was transferred to a Teflon-lined autoclave (100 mL) and heated in oven for 12 h (180 °C). After cooling to room temperature, the obtained mixture was filtered through a PTFE membrane with 0.2 μm pore diameter. The composites were washed four times with 100 mL of $H_2O$ and freeze-dried in vacuum.

#### 2.1.3 *Synthesis of MWCNTs–$Fe_3O_4$+rGO (F-3)*

To maintain the same synthesized parameters, reduced graphene oxide (rGO) was prepared through the same procedure as the F-2 except the MWCNTs and Fe(acac)$_3$ were not added into the ethylene glycol–triethylene glycol solution. Then, the obtained rGO was mixed with 116 mg of F-1 in 20 mL of $H_2O$ for 1 h. Finally, the obtained mixture was filtered through a

PTFE membrane with 0.2 μm pore diameter. The composites were washed four times with 100 mL $H_2O$ and freeze-dried in vacuum.

### 2.1.4 *Synthesis of rGO-$Fe_3O_4$ (F-4)*

Firstly, graphene oxide (GO) solution was prepared through mixing 2.5 mL of 5 mg/mL GO with 5 mL of ethylene glycol. Secondly, 400 mg of $Fe(acac)_3$ was added to a 50 mL flask containing 24 mL of triethylene glycol (TREG). After ultrasonication for 10 min, the resulting solution was rapidly heated to 190 °C under argon protection, maintained there for 30 min, and then heated rapidly to 278 °C, and held there for an additional 30 min. After cooling to room temperature, the obtained $Fe_3O_4$ was stirred directly with the above-mentioned GO solution for 1 h. Then, the mixture was transfered to a Teflon-lined autoclave (100 mL) and heated in oven for 12 h (180 °C). After cooling to room temperature, the obtained mixture was filtered through a PTFE membrane with 0.2 μm pore diameter. The composites were washed four times with 100 mL $H_2O$ and freeze-dried in vacuum.

## 2.2 Characterization

### 2.2.1 *Materials characterization*

X-ray diffraction (XRD) patterns were recorded on a Rigaku D/max-2500 diffractometer with Cu K$\alpha$ radiation ($\lambda$ = 1.5418 Å) at 40 kV and 200 mA. The morphology and microstructures of the samples were characterized by scanning electron microscopy (HITACHI S-4800 SEM), transmission electron microscopy (TEM, JEOL-1011) and high-resolution transmission electron microscopy (HRTEM) (JEOL, JEM-2100F). X-ray photoelectron spectroscopy (XPS) measurements were performed on the VG Scientific ESCALab220i-XL spectrometer using Al K$\alpha$ radiation. The loading content of Fe was determined by inductively coupled plasma–atomic emission spectroscopy (ICP–AES) (VISTA-MPX). Thermogravimetric analysis (TGA) was carried out on a Shimadzu DTG-60H instrument under a flow of air with a temperature ramp of 5 °C/min from room temperature to 850 °C. Fourier transform infrared (FT-IR) spectra were obtained using a Bruker Tensor 27 spectrometer using pressed KBr pellets to test the chemical bonding of the products from 400 to 4,000 $cm^{-1}$. Raman spectra were measured on a Thermo Scientific DXR spectrometer (excited by 532 nm He–Ne laser).

### 2.2.2 *Electrochemical characterization*

Electrochemical experiments were performed using Swagelok-type cells. To prepare working electrodes, active material, Super-P carbon black, and poly(vinylidene fluoride) (PVDF) with mass ratio 80:10:10 were mixed into a homogeneous slurry in *N*-methylpyrrolidone (NMP) with a pestle and mortar. The obtained slurry was pasted onto pure Cu foil (99.9%, Goodfellow). The mass loading of the working electrode materials was about 1.3 $mg/cm^2$. The electrolyte was 1 M $LiPF_6$ in ethylene carbonate/dimethyl carbonate (EC/DMC, 1:1 *v*/*v*) (Novolyte Technologies). Glass fibers (GF/D) from Whatman were used as separators and pure lithium metal foil (Aldrich) was used as the counter electrode. Cell assembly was carried out in an Ar-filled glovebox with concentrations of moisture and oxygen below 1.0 ppm. It should be pointed out that the specific capacity values are calculated on the basis of total mass of the MWCNTs–$Fe_3O_4$–rGO hybrid. The charge and discharge measurements of the batteries were carried out on an Arbin BT2000 system in the fixed voltage window between 5 mV and 3 V vs $Li^+/Li$ at room temperature. Electrochemical impedance spectroscopy was performed on a PARSTAT 2273 advanced electrochemical system (Princeton Applied Research) over the frequency range from 100 kHz to 10 MHz.

# 3 Results and discussion

A schematic illustration of the synthesis route for the MWCNTs–$Fe_3O_4$–rGO nanocomposites is shown in Fig. 1. $Fe_3O_4$ nanoparticles were first coated directly onto the surface of pristine MWCNTs through one-pot thermolysis of $Fe(acac)_3$ in triethylene glycol (TREG), as reported previously [38]. The resulting MWCNTs–$Fe_3O_4$ (denoted as F-1) was mixed with GO–ethylene glycol solution, and then treated solvothermally at 180 °C for 5 h. The obtained black products were washed several times with $H_2O$ and then freeze-dried to produce the MWCNTs–$Fe_3O_4$–rGO (denoted as F-2) nanocomposites. Under the solvothermal conditions, GO was gradually reduced by

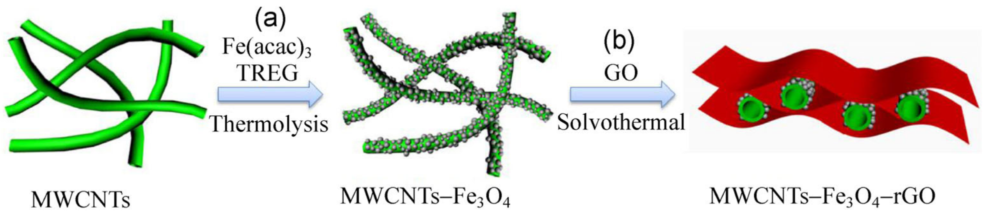

**Figure 1** Schematic illustration of the synthesis route for the MWCNTs–$Fe_3O_4$–rGO (F-2) nanocomposites: (a) One-pot synthesis of $Fe_3O_4$ nanoparticles decorated on the surface of MWCNTs without pretreatment; (b) solvothermal of MWCNTs–$Fe_3O_4$ (F-1) with GO in ethylene glycol solution to produce MWCNTs–$Fe_3O_4$–rGO (F-2).

ethylene glycol and wrapped MWCNTs–$Fe_3O_4$ to form rGO networks.

The typical XRD pattern of MWCNTs–$Fe_3O_4$ (F-1) is displayed in Fig. 2(a), in which all of diffraction peaks are in good agreement with the standard patterns for $Fe_3O_4$ (JCPDS No. 99-0073) and MWCNTs. No other characteristic peaks from impurities were detected. No obvious difference in the XRD pattern was found after rGO wrapping, indicating that the phase structures were maintained. The reflection peak of rGO should be at 23.5°, and this position is obscured by the characteristic peak of MWCNTs. Due to the similar XRD patterns of $Fe_3O_4$ and $\gamma$-$Fe_2O_3$, X-ray photoelectron spectroscopy (XPS) analysis was conducted to further confirm that $Fe_3O_4$ was not oxidized. Figure S1 (in the Electronic Supplementary Material (ESM)) presents the Fe 2p high-resolution XPS spectra of the nanocomposites. The two broad peaks around 710.9 and 724.5 eV are typical characteristics of $Fe_3O_4$ [16, 39], and no satellite peak of $\gamma$-$Fe_2O_3$ around 719.2 eV was observed in the spectra of either the MWCNTs–$Fe_3O_4$ (F-1) or MWCNTs–$Fe_3O_4$–rGO (F-2) samples. Figure S2 (in the ESM) shows the FT-IR spectrum of MWCNTs–$Fe_3O_4$–rGO (F-2). It can be seen the carboxyl peak at 1,732 cm$^{-1}$ disappeared after solvothermal treatment in ethylene glycol. In addition, hydroxyl group peaks at around 3,400 and 1,112 cm$^{-1}$ decreased in intensity. Both these observations suggest the reduction of GO [40]. Raman spectroscopy was employed to further confirm the reduction of GO (Fig. 2(b)). The D band (disordered induced phonon mode) at 1,343 cm$^{-1}$ and G band (graphite band) at 1,601 cm$^{-1}$ of carbon can be clearly seen in the spectra of both MWCNTs–$Fe_3O_4$ (F-1) and MWCNTs–$Fe_3O_4$–rGO (F-2). The intensity ratio $I_D/I_G$ changed from 0.82 for MWCNTs–$Fe_3O_4$ (F-1) to 1.12 after wrapping with rGO. The slight increase in $I_D/I_G$ can be ascribed to weaker degree of graphitization of rGO obtained by reduction in ethylene glycol solution compared to pristine MWCNTs obtained by the chemical vapor deposition (CVD) method.

The morphology and microstructure of MWCNTs–$Fe_3O_4$ (F-1) and MWCNTs–$Fe_3O_4$–rGO (F-2) were examined via scanning electron microscopy (SEM), transmission electron microscopy (TEM), and high-resolution TEM (HRTEM). Figure 3(a) shows a typical

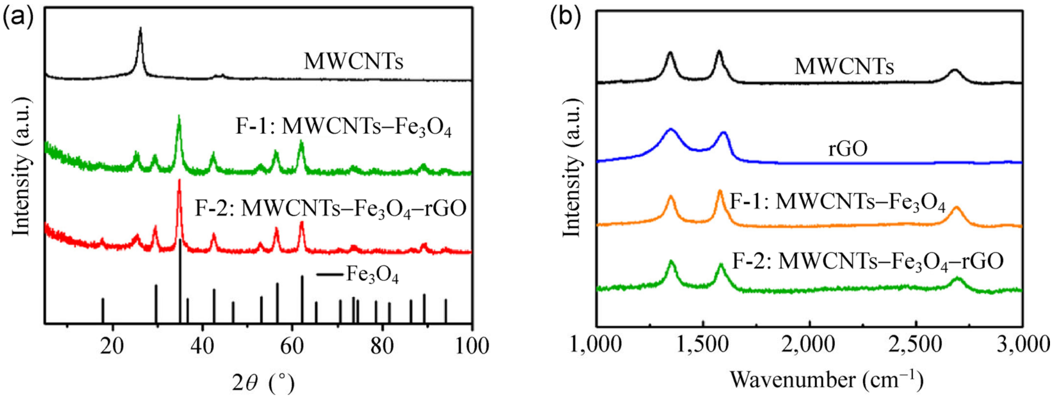

**Figure 2** (a) XRD patterns and (b) Raman spectra of MWCNTs–$Fe_3O_4$ (F-1) and MWCNTs–$Fe_3O_4$–rGO (F-2) nanocomposites.

low-magnification SEM image of the MWCNTs–$Fe_3O_4$ (F-1). The surface of MWCNTs was indeed very rough, indicating a large number of $Fe_3O_4$ nanoparticles were decorated onto the surface of MWCNTs. TEM image (Fig. 3(b)) further confirms $Fe_3O_4$ nanoparticles with diameter of ca. 7 nm were uniformly dispersed on the surface of MWCNTs. In the HRTEM image (Fig. S3 in the ESM), crystalline planes of $Fe_3O_4$ as well as MWCNTs can be clearly seen. The SEM and TEM images of MWCNTs–$Fe_3O_4$–rGO (F-2) are shown in Figs. 3(c) and 3(d). From the SEM image, it can be seen that MWCNTs–$Fe_3O_4$ (F-1) nanocomposites were wrapped well with rGO after solvothermal treatment of MWCNTs–$Fe_3O_4$ (F-1) with GO in ethylene glycol solution. Note that $Fe_3O_4$ nanoparticles are still attached on the surface of MWCNTs (Fig. 3(d)). No obvious $Fe_3O_4$ nanoparticles were observed on rGO, indicating $Fe_3O_4$ nanoparticles were decorated tightly on the surface of MWCNTs. For comparison, a physical mixture of MWCNTs–$Fe_3O_4$ (F-1) with rGO only produced separated structures (as shown in Fig. S4 in the ESM). The interactions between $Fe_3O_4$ and the untreated MWCNTs are still unclear, while there is chemical binding between rGO and $Fe_3O_4$ in F-2. During the solvothermal process, part of the ethylene glycol molecules could react with the surface of GO, which contain abundant oxygen-containing groups, serving as cross-linking sites to wrap the MWCNTs–$Fe_3O_4$ (F-1) to form rGO networks [14, 41].

ICP–AES analysis results showed that the $Fe_3O_4$ loadings were 53.4 wt.% and 52.3 wt.%, respectively, in MWCNTs–$Fe_3O_4$ (F-1) and MWCNTs–$Fe_3O_4$–rGO (F-2); these values are very close to those in the synthesis mixtures (Table S1 in the ESM). TGA, carried out in air at a heating rate of 5 °C·min$^{-1}$, also confirmed that there was about 53 wt.% $Fe_3O_4$ in the final MWCNTs–$Fe_3O_4$–rGO (F-2) nanocomposites ($Fe_2O_3$ is assumed to be the final product, and the content of $Fe_3O_4$ could be deduced from the amount of $Fe_2O_3$, as shown in Fig. S5 in the ESM).

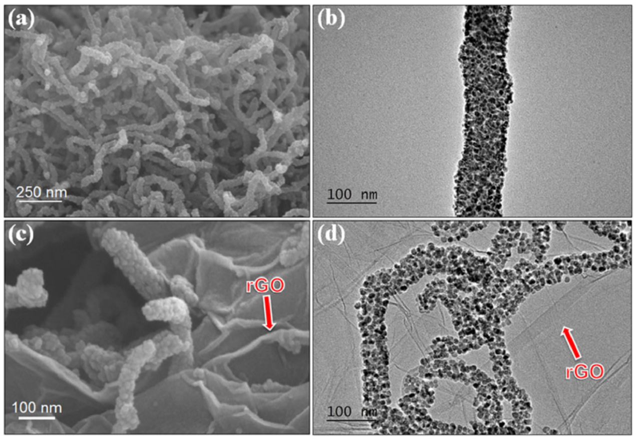

**Figure 3** (a) SEM and (b) TEM images of MWCNTs–$Fe_3O_4$ (F-1); (c) SEM and (d) TEM images of MWCNTs–$Fe_3O_4$–rGO (F-2) nanocomposites.

Galvanostatic discharge–charge measurements were used to test the electrochemical performance of the MWCNTs–$Fe_3O_4$–rGO (F-2) nanocomposites. The discharge–charge voltage profiles under a current density of 200 mA·g$^{-1}$ over the voltage range 0–3.0 V of MWCNTs–$Fe_3O_4$–rGO (F-2) nanocomposites is shown in Fig. 4(a). It can be calculated that the initial discharge and charge specific capacities of the MWCNTs–$Fe_3O_4$–rGO nanocomposite are 1,277 and 780 mA·h·g$^{-1}$, respectively. The large initial discharge capacity of the nanocomposites could be attributed to the small size of $Fe_3O_4$ nanoparticles. However, a large irreversible capacity loss due to the formation of solid electrolyte interface (SEI) films between electrolyte and the surface of $Fe_3O_4$ was observed, resulting in the low coulombic efficiency in the first cycle [16, 42]. In addition, the small size of $Fe_3O_4$ nanoparticles in MWCNTs–$Fe_3O_4$–rGO (F-2) nanocomposites leads to the formation of SEI films to a greater extent. One possible way to improve the coulombic efficiency in the first cycle is to carbon coat the $Fe_3O_4$ nanoparticles first.

For comparison, MWCNTs–$Fe_3O_4$ (F-1) without rGO and a physical mixture of MWCNTs–$Fe_3O_4$ and rGO (MWCNTs–$Fe_3O_4$+rGO, denoted as F-3, see Table S1 and Figs. S4–S6 in the ESM), $Fe_3O_4$–rGO (denoted as F-4, see Table S1 and Figs. S7 and S8 in the ESM) were also prepared and tested. As shown in Fig. S9 in the ESM, although MWCNTs–$Fe_3O_4$ (F-1) showed a high first discharge capacity (1,265 mA·h·g$^{-1}$), the capacity decayed quickly and only 97 mA·h·g$^{-1}$ was maintained after 11th run (Fig. S9(a) in the ESM). After physical addition of rGO, the resulting MWCNTs–$Fe_3O_4$+rGO (F-3) exhibited a higher specific capacity than MWCNTs–$Fe_3O_4$ (F-1). However, a capacity of only 200 mA·h·g$^{-1}$ was maintained after the 50th cycle, which is much lower than that of MWCNTs–$Fe_3O_4$–

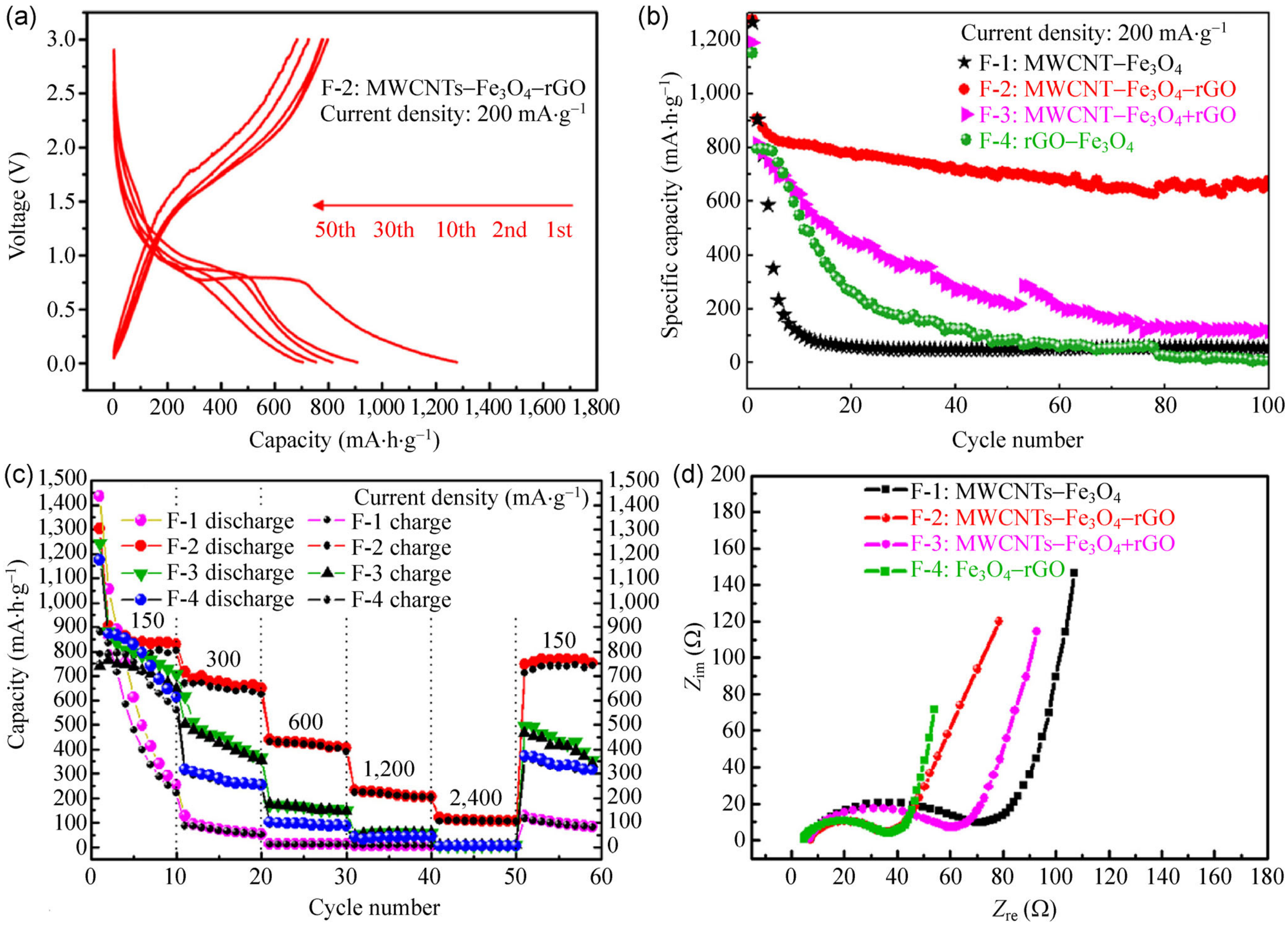

**Figure 4** (a) Charge–discharge curves of F-2 nanocomposites cycled at 0–3.0 V at a current density of 200 mA·g$^{-1}$; (b) cycling behavior at a current density of 200 mA·g$^{-1}$; (c) rate performances under different current densities and (d) Nyquist plots of the electrode of F-1, F-2, F-3, and F-4.

rGO (F-2) nanocomposites (Fig. S9(b) in the ESM). At the same time, $Fe_3O_4$–rGO (F-4) with a uniform distribution of $Fe_3O_4$ nanoparticles on rGO was also prepared using GO instead of MWCNTs (Figs. S7 and S8 in the ESM). As shown in Fig. 4(b), $Fe_3O_4$–rGO (F-4) exhibited a rapid decay of capacity. However, the MWCNTs–$Fe_3O_4$–rGO (F-2) nanocomposites still retained a reversible capacity of ~680 mA·h·g$^{-1}$ after 100 cycles under a current density of 200 mA·g$^{-1}$, whereas the MWCNTs–$Fe_3O_4$ (F-1) and MWCNTs–$Fe_3O_4$+rGO (F-3) only showed specific capacities as low as 54 and 115 mA·h·g$^{-1}$, respectively. The minor capacity decay of MWCNTs–$Fe_3O_4$–rGO (F-2) can be ascribed to that part of the $Fe_3O_4$ nanoparticles detached from the MWCNTs during charge–discharge processes. In F-2, the binding contact between MWCNTs and $Fe_3O_4$ nanoparticles is not very strong because the MWCNTs were not functionalized. Compared with other work, this capacity is not the best reported, but is still relatively high.

Comparison with the MWCNTs–$Fe_3O_4$ (F-1), MWCNTs–$Fe_3O_4$+rGO (F-3) and $Fe_3O_4$–rGO (F-4), MWCNTs–$Fe_3O_4$–rGO (F-2) nanocomposites also showed considerable improvement of the rate capability. As shown in Fig. 4(c), the MWCNTs–$Fe_3O_4$–rGO (F-2) nanocomposites show a much higher capacity than other three control samples at all investigated current densities. The much improved electrochemical performance of the MWCNTs–$Fe_3O_4$–rGO (F-2) nanocomposites could be attributed to the unique structure with double protection afforded by MWCNTs and rGO networks. First, the MWCNTs act as a carrier for direct decoration and combination of $Fe_3O_4$ nanoparticles, forming conducting wires and facilitating the electron transmission. In addition, MWNCTs were not treated by any strong acid or modified by heteroatoms in this work. The intact structure of MWCNTs is beneficial for maintaining a perfect conjugated structure, which is ideal for the electron transfer during the charge–discharge process. Second, the rGO networks serve as not only the elastic buffer protection for volume expansion of the $Fe_3O_4$ upon lithium insertion, but also as an electronically conducting substrate, inducing further improvement of electrical conductivity of the overall electrode. It can be seen that most of $Fe_3O_4$ nanoparticles with small size were still attached on the surface of MWCNTs, and the overall structure of MWCNTs–$Fe_3O_4$–rGO (F-2) was maintained well after cycling (Fig. S10 in the ESM). However, MWCNTs–$Fe_3O_4$ without rGO, physically mixed with rGO, or $Fe_3O_4$–rGO showed aggregation and detachment of $Fe_3O_4$ nanoparticles during the charge–discharge cycling process (Figs. S11–S13 in the ESM).

Electrochemical impedance spectroscopy (EIS) further confirmed the enhanced electrical conductivity of the MWCNTs–$Fe_3O_4$–rGO (F-2) nanocomposites. The Nyquist plots of different samples are shown in Fig. 4(d). The semicircle in the middle frequency range indicates the charge transfer resistance $R_{ct}$ relating to charge transfer through the electrode/electrolyte interface [9, 13, 43]. It can be clearly seen that the MWCNTs–$Fe_3O_4$–rGO (F-2) electrode showed a much lower charge transfer resistance $R_{ct}$ than MWCNTs–$Fe_3O_4$ (F-1) or MWCNTs–$Fe_3O_4$+rGO (F-3), while having a similar resistance $R_{ct}$ to that of $Fe_3O_4$–rGO (F-4).

## 4 Conclusions

We have developed a facile two-step method to produce MWCNTs–$Fe_3O_4$–rGO (F-2) nanocomposites with double protection afforded by $Fe_3O_4$ nanoparticles through the use of MWCNTs and rGO networks. The resulting MWCNTs–$Fe_3O_4$–rGO (F-2) nanocomposites exhibited significantly improved electrochemical performance in comparison with MWCNTs–$Fe_3O_4$ (F-1), MWCNTs–$Fe_3O_4$+rGO (F-3), and $Fe_3O_4$–rGO (F-4) when used as an anode material for Li-ion batteries. The excellent properties can be attributed to the electronically conductive nature of the MWCNTs and rGO networks as well as the elasticity of rGO and the small size of the $Fe_3O_4$ nanoparticles. We believe this double protection strategy can be extended to other materials with large volume variations and low electrical conductivities.

## Acknowledgements

We thank the National Basic Research Program of China (Grant No. 2012CB932900), the National Natural Science Foundation of China (NSFC Grants Nos. 21121063 and 51225204), and the Chinese Academy of Sciences (Grant No. KJCX2-YW-N41) for financial support.

**Electronic Supplementary Material**: Supplementary material (additional characterization of the MWCNTs–$Fe_3O_4$ (F-1), MWCNTs–$Fe_3O_4$–rGO (F-2), MWCNTs–$Fe_3O_4$+rGO (F-3) and $Fe_3O_4$–rGO (F-4)) is available in the online version of this article at http://dx.doi.org/10.1007/s12274-014-0625-6.

## References

[1] Wang, Z.; Zhou, L.; Lou, X. W. Metal oxide hollow nanostructures for lithium-ion batteries. *Adv. Mater.* **2012**, *24*, 1903–1911.

[2] Tarascon, J. M.; Armand, M. Issues and challenges facing rechargeable lithium batteries. *Nature* **2001**, *414*, 359–367.

[3] Poizot, P.; Laruelle, S.; Grugeon, S.; Dupont, L.; Tarascon, J. M. Nano-sized transition-metal oxides as negative-electrode materials for lithium-ion batteries. *Nature* **2000**, *407*, 496–499.

[4] Xu, S.; Hessel, C. M.; Ren, H.; Yu, R.; Jin, Q.; Yang, M.; Zhao, H.; Wang, D. $\alpha$-$Fe_2O_3$ multi-shelled hollow microspheres for lithium ion battery anodes with superior capacity and charge retention. *Energy Environ. Sci.* **2014**, *7*, 632–637.

[5] Wang, J.; Yang, N.; Tang, H.; Dong, Z.; Jin, Q.; Yang, M.; Kisailus, D.; Zhao, H.; Tang, Z.; Wang, D. Accurate control of multishelled $Co_3O_4$ hollow microspheres as high-performance anode materials in lithium-ion batteries. *Angew. Chem. Int. Ed.* **2013**, *52*, 6417–6420.

[6] Zhang, L.; Wu, H. B.; Lou, X. W. Iron-oxide-based advanced anode materials for lithium-ion batteries. *Adv. Energy Mater.* **2014**, *4*, 1300958.

[7] Chen, Y.; Song, B.; Tang, X.; Lu, L.; Xue, J. Ultrasmall $Fe_3O_4$ nanoparticle/$MoS_2$ nanosheet composites with superior

performances for lithium ion batteries. *Small* **2014**, *10*, 1536–1543.

[8] Chen, D.; Ji, G.; Ma, Y.; Lee, J. Y.; Lu, J. Graphene-encapsulated hollow $Fe_3O_4$ nanoparticle aggregates as a high-performance anode material for lithium ion batteries. *ACS Appl. Mater. Interfaces* **2011**, *3*, 3078–3083.

[9] Wang, J.-Z.; Zhong, C.; Wexler, D.; Idris, N. H.; Wang, Z.-X.; Chen, L.-Q.; Liu, H.-K. Graphene-encapsulated $Fe_3O_4$ nanoparticles with 3D laminated structure as superior anode in lithium ion batteries. *Chem. Eur. J.* **2011**, *17*, 661–667.

[10] Zhou, G.; Wang, D.-W.; Li, F.; Zhang, L.; Li, N.; Wu, Z.-S.; Wen, L.; Lu, G. Q.; Cheng, H.-M. Graphene-wrapped $Fe_3O_4$ anode material with improved reversible capacity and cyclic stability for lithium ion batteries. *Chem. Mater.* **2010**, *22*, 5306–5313.

[11] Ji, L.; Tan, Z.; Kuykendall, T. R.; Aloni, S.; Xun, S.; Lin, E.; Battaglia, V.; Zhang, Y. $Fe_3O_4$ nanoparticle-integrated graphene sheets for high-performance half and full lithium ion cells. *Phys. Chem. Chem. Phys.* **2011**, *13*, 7170–7177.

[12] Zhang, M.; Lei, D.; Yin, X.; Chen, L.; Li, Q.; Wang, Y.; Wang, T. Magnetite/graphene composites: Microwave irradiation synthesis and enhanced cycling and rate performances for lithium ion batteries. *J. Mater. Chem.* **2010**, *20*, 5538–5543.

[13] Yang, S.; Feng, X.; Ivanovici, S.; Müllen, K. Fabrication of graphene-encapsulated oxide nanoparticles: Towards high-performance anode materials for lithium storage. *Angew. Chem. Int. Ed.* **2010**, *49*, 8408–8411.

[14] Wei, W.; Yang, S.; Zhou, H.; Lieberwirth, I.; Feng, X.; Müllen, K. 3D graphene foams cross-linked with pre-encapsulated $Fe_3O_4$ nanospheres for enhanced lithium storage. *Adv. Mater.* **2013**, *25*, 2909–2914.

[15] Su, Y.; Li, S.; Wu, D.; Zhang, F.; Liang, H.; Gao, P.; Cheng, C.; Feng, X. Two-dimensional carbon-coated graphene/metal oxide hybrids for enhanced lithium storage. *ACS Nano* **2012**, *6*, 8349–8356.

[16] Su, J.; Cao, M.; Ren, L.; Hu, C. $Fe_3O_4$–graphene nanocomposites with improved lithium storage and magnetism properties. *J. Phys. Chem. C* **2011**, *115*, 14469–14477.

[17] Luo, J.; Liu, J.; Zeng, Z.; Ng, C. F.; Ma, L.; Zhang, H.; Lin, J.; Shen, Z.; Fan, H. J. Three-dimensional graphene foam supported $Fe_3O_4$ lithium battery anodes with long cycle life and high rate capability. *Nano Lett.* **2013**, *13*, 6136–6143.

[18] Li, B.; Cao, H.; Shao, J.; Qu, M.; Warner, J. H. Superparamagnetic $Fe_3O_4$ nanocrystals@graphene composites for energy storage devices. *J. Mater. Chem.* **2011**, *21*, 5069–5075.

[19] Bhuvaneswari, S.; Pratheeksha, P. M.; Anandan, S.; Rangappa, D.; Gopalan, R.; Rao, T. N. Efficient reduced graphene oxide grafted porous $Fe_3O_4$ composite as a high performance anode material for Li-ion batteries. *Phys. Chem. Chem. Phys.* **2014**, *16*, 5284–5294.

[20] Sathish, M.; Tomai, T.; Honma, I. Graphene anchored with $Fe_3O_4$ nanoparticles as anode for enhanced Li-ion storage. *J. Power Sources* **2012**, *217*, 85–91.

[21] Kang, E.; Jung, Y. S.; Cavanagh, A. S.; Kim, G.-H.; George, S. M.; Dillon, A. C.; Kim, J. K.; Lee, J. $Fe_3O_4$ nanoparticles confined in mesocellular carbon foam for high performance anode materials for lithium-ion batteries. *Adv. Funct. Mater.* **2011**, *21*, 2430–2438.

[22] Wang, L.; Yu, Y.; Chen, P. C.; Zhang, D. W.; Chen, C. H. Electrospinning synthesis of C/$Fe_3O_4$ composite nanofibers and their application for high performance lithium-ion batteries. *J. Power Sources* **2008**, *183*, 717–723.

[23] Cui, Z.-M.; Jiang, L.-Y.; Song, W.-G.; Guo, Y.-G. High-yield gas-liquid interfacial synthesis of highly dispersed $Fe_3O_4$ nanocrystals and their application in lithium-ion batteries. *Chem. Mater.* **2009**, *21*, 1162–1166.

[24] Wang, Y.; Zhang, L.; Gao, X.; Mao, L.; Hu, Y.; Lou, X. W. One-pot magnetic field induced formation of $Fe_3O_4$/C composite microrods with enhanced lithium storage capability. *Small* **2014**, *10*, 2815–2819.

[25] Dai, H. Carbon nanotubes: Synthesis, integration, and properties. *Acc. Chem. Res.* **2002**, *35*, 1035–1044.

[26] Baughman, R. H. Carbon nanotubes—the route toward applications. *Science* **2002**, *297*, 787–792.

[27] Wang, S.; Yi, L.; Halpert, J. E.; Lai, X.; Liu, Y.; Cao, H.; Yu, R.; Wang, D.; Li, Y. A novel and highly efficient photocatalyst based on P25–graphdiyne nanocomposite. *Small* **2012**, *8*, 265–271.

[28] Wassei, J. K.; Kaner, R. B. Oh, the places you'll go with graphene. *Acc. Chem. Res.* **2013**, *46*, 2244–2253.

[29] Huang, X.; Qi, X; Boey, F.; Zhang, H. Graphene-based composites. *Chem. Soc. Rev.* **2012**, *41*, 666–686.

[30] Tang, H.; Hessel, C. M.; Wang, J.; Yang, N.; Yu, R.; Zhao, H.; Wang, D. Two-dimensional carbon leading to new photoconversion processes. *Chem. Soc. Rev.* **2014**, *43*, 4281–4299.

[31] Tang, H.; Yin, H.; Wang, J.; Yang, N.; Wang, D.; Tang, Z. Molecular architecture of cobalt porphyrin multilayers on reduced graphene oxide sheets for high-performance oxygen reduction reaction. *Angew. Chem. Int. Ed.* **2013**, *52*, 5585–5589.

[32] Yang, N.; Liu, Y.; Wen, H.; Tang, Z.; Zhao, H.; Li, Y.; Wang, D. Photocatalytic properties of graphdiyne and graphene modified $TiO_2$: From theory to experiment. *ACS Nano* **2013**, *7*, 1504–1512.

[33] Cheng, J.; Wang, B.; Park, C.-M.; Wu, Y.; Huang, H; Nie, F. CNT@$Fe_3O_4$@C coaxial nanocables: One-pot, additive-

free synthesis and remarkable lithium storage behavior. *Chem. Eur. J.* **2013**, *19*, 9866–9874.

[34] Ban, C.; Wu, Z.; Gillaspie, D. T.; Chen, L.; Yan, Y.; Blackburn, J. L.; Dillon, A. C. Nanostructured $Fe_3O_4$/SWNT electrode: Binder-free and high-rate Li-ion anode. *Adv. Mater.* **2010**, *22*, E145–E149.

[35] Jian, Z.; Liu, P.; Li, F.; He, P.; Guo, X.; Chen, M.; Zhou, H. Core–shell-structured CNT@$RuO_2$ composite as a high-performance cathode catalyst for rechargeable Li–$O_2$ batteries. *Angew. Chem. Int. Ed.* **2013**, *53*, 442–446.

[36] Shi, Q.; Peng, F.; Liao, S.; Wang, H.; Yu, H.; Liu, Z.; Zhang, B.; Su, D. S. Sulfur and nitrogen co-doped carbon nanotubes for enhancing electrochemical oxygen reduction activity in acidic and alkaline media. *J. Mater. Chem. A* **2013**, *1*, 14853–14857.

[37] Chen, C.; Zhang, J.; Zhang, B.; Yu, C.; Peng, F.; Su, D. Revealing the enhanced catalytic activity of nitrogen-doped carbon nanotubes for oxidative dehydrogenation of propane. *Chem. Commun.* **2013**, *49*, 8151–8153.

[38] Cao, C.-Y.; Wei, F.; Qu, J.; Song, W.-G. Programmed synthesis of magnetic magnesium silicate nanotubes with high adsorption capacities for lead and cadmium ions. *Chem. Eur. J.* **2013**, *19*, 1558–1562.

[39] Fujii, T.; de Groot, F. M. F.; Sawatzky, G. A.; Voogt, F. C.; Hibma, T.; Okada, K. *In situ* XPS analysis of various iron oxide films grown by $NO_2$-assisted molecular-beam epitaxy. *Phys. Rev. B* **1999**, *59*, 3195–3202.

[40] Arif Sher Shah, M. S.; Zhang, K.; Park, A. R.; Kim, K. S.; Park, N.-G.; Park, J. H.; Yoo, P. J. Single-step solvothermal synthesis of mesoporous Ag–$TiO_2$–reduced graphene oxide ternary composites with enhanced photocatalytic activity. *Nanoscale* **2013**, *5*, 5093–5101.

[41] Yu, Y.; Sun, Y.; Cao, C.; Yang, S.; Liu, H.; Li, P.; Huang, P.; Song, W. Graphene-based composite supercapacitor electrodes with diethylene glycol as inter-layer spacer. *J. Mater. Chem. A* **2014**, *2*, 7706–7710.

[42] Li, B.; Cao, H.; Shao, J.; Qu, M. Enhanced anode performances of the $Fe_3O_4$–carbon–rGO three dimensional composite in lithium ion batteries. *Chem. Commun.* **2011**, *47*, 10374–10376.

[43] Tu, W.; Zhou, Y.; Zou, Z. Versatile graphene-promoting photocatalytic performance of semiconductors: Basic principles, synthesis, solar energy conversion, and environmental applications. *Adv. Funct. Mater.* **2013**, *23*, 4996–5008.